Supplementary Information for
Timeline of lunar differentiation recorded in Ca and Mg stable isotopes

Hairuo Fu[1*], Stein B. Jacobsen[1], Fatemeh Sedaghatpour[1]

[1]Department of Earth and Planetary Sciences, Harvard University, Cambridge, MA 02138, USA.

*Corresponding author: Hairuo Fu (hairuo.fu@g.harvard.edu)

This file includes:

Supplementary Text (section 1 to 3)
Figures 1 to 5
Tables 1 to 8
Supplementary References

Supplementary Text

1) Inversion for the BSM Ca-isotope composition

To constrain the BSM Ca-isotope value, we develop the LMO isotopic fractionation model upon the structures established in Sedaghatpour and Jacobsen (*1*) and Fu et al. (*2*). First, we select two representative chemical models for the LMO crystallization from Schmidt and Kraettli (*3*) Snyder et al. (*4*).

The classic shallow-LMO mineral sequence from Snyder et al. (*4*) was obtained by thermodynamic modeling that computed equilibrium phase relations throughout the LMO solidification. The resolved evolving phase transitions are (i) olivine (0–40%); (ii) orthopyroxene (40–78%); (iii) olivine + pigeonite + plagioclase (78–86%); (iv) pigeonite + plagioclase + clinopyroxene (86–95%); (v) pigeonite + clinopyroxene + plagioclase + ilmenite (95–99.5%) (Table 2). The first 0–76% LMO solidification is assumed to be equilibrium crystallization, and the rest (76–99.5%) is fractional crystallization, reflecting the presumably less dynamic convection of the LMO that facilitated crystal settling as the magma cooled and the lunar insulating anorthosite lid started to form.

The experimental deep-LMO crystallization sequence was recently established by Schmidt and Kraettli (*3*). The experiments started with a similar bulk silicate Moon chemical composition (Taylor Whole Moon composition) (*5*) to that used in Snyder et al. (*4*) and temperature and pressure conditions for an 1,150-km deep primordial LMO. The mineral phases and mass proportions are tabulated in Table 3. Major differences between this experimental model and the thermodynamic model (*4*) include: (i) the main Fe-Ti oxide obtained from the experiments was spinel instead of ilmenite; (ii) no pigeonite crystallized from the experimental melts; (iii) plagioclase started to be a saturated phase since 70% of LMO crystallization in the experiments, contrasting to at ~78% determined by the thermodynamic model; (iv) the experiments simulated solely fractional crystallization for the LMO solidification. In Schmidt and Kraettli (*4*), a synthesis of four existing LMO crystallization experimental studies (*4*, *6–8*) found that, although different in detail in the selection of BSM chemical compositions and the resulted crystallization paths, all experiments similarly converged on a common sequence of major phases: olivine – orthopyroxene – clinopyroxene + plagioclase – quartz + Fe-Ti oxide. Therefore, the selected experimental (*3*) and thermodynamic (*4*) models cover sufficiently the broad scenarios of the LMO crystallization and make a valuable set of sensitivity tests to understand the LMO isotopic compositions reliably.

Because the isotope fractionation effect is highly temperature dependent (proportional to the inversed square of temperature), it is important to account for the crystallization temperature variation throughout the LMO crystallization. We take the LMO crystallization temperature profile determined by the experimental models, assuming crystallization for an 1,150 km-deep-LMO (*3*) and 600 km-shallow-LMO (*7*). We plotted their reported crystallization temperature versus degree of LMO crystallization (1-*F*,), where *F* is the LMO residual melt fraction) and fit them with polynomial functions (Fig. 2), which we use for the isotopic modeling of the deep-LMO:

$$T\,(^{\circ}C) = -2435.6F^4 + 4282.8F^3 - 2033.6F^2 + 1015.1F + 1041.8 \quad \textbf{(S1)}$$

And for the shallow-LMO:

$$T\,(°C) = -34.3F^3 - 136.4F^2 + 900.1F + 1095.0 \quad \textbf{(S2)}$$

To model the Ca isotopic evolution of the LMO, we implement a Monte Carlo isotopic fractionation model developed by Fu et al. (*2*) (described in more detail in **Section 3: Mg and Ca isotopic fractionation models with a Monte Carlo method**), which can account for propagated errors surrounding the initial isotopic composition and temperature-dependent fractionation factors. The temperature-dependent mineral-melt Ca-isotope fractionation factors used for modeling are provided in Table 5. The bulk mineral partition coefficient (D^{Ca}) for each crystallization stage is parameterized (Tables 2 and 3) such that the Ca concentration variation reproduces that reported by Schmidt and Kraettli (*3*) and Snyder et al. (*4*) (Fig. 3). We categorize the fractionating cumulates into sinking cumulates (heavy minerals including olivine, orthopyroxene, pigeonite, clinopyroxene, ilmenite, and spinel) and flotation cumulates (plagioclase).

As an initial test, we assume the BSM has the same Ca-isotope composition as the BSE (0.94 ± 0.05‰) (*9*), similar to those that have been observed for Mg and Fe isotopes (*1*, *10*). With this initial $\delta^{44/40}$Ca, for the experimental deep-LMO model, the modeled mean $\delta^{44/40}$Ca of the instantaneous floatation cumulates evolves from 0.841‰ to 0.590‰ between 69.9% and 99.9% LMO crystallization, averaging at 0.821 ± 0.103‰ (two standard deviations, 2SD) (Fig. 4a). For the thermodynamic shallow-LMO model, the mean $\delta^{44/40}$Ca value of floatation cumulates changes from 0.793‰ to 0.719‰ between 78% and 99.5% LMO crystallization, averaging at 0.786 ± 0.036 ‰ (Fig. 4b). Both modeled averages of flotation cumulate overlap with the measured mean $\delta^{44/40}$Ca for highland FANs and feldspathic breccias from this study and the literature (0.763 ± 0.044‰, 2SD, n = 13) within uncertainty. Such a comparison suggests that assuming the BSM $\delta^{44/40}$Ca is identical to the BSE could reproduce, if not accurately enough, the observed $\delta^{44/40}$Ca for the lunar crust.

Assuming that these floatation cumulate samples represent the average lunar crust, we develop an inversion model to back-constrain the accurate BSM $\delta^{44/40}$Ca value (i.e., the initial LMO $\delta^{44/40}$Ca). First, we draw 10,000 random initial LMO $\delta^{44/40}$Ca values from normal distributions spanning from 0.8–1.2‰, a broad range for testing. Each initial $\delta^{44/40}$Ca, paired with a set of fractionation factors simulated by a Monte Carlo approach (*2*), generates an individual evolutionary curve for the LMO (purple line) and its equilibrium instantaneous floatation cumulates (grey line) in the evolved differentiation stages (69.9–99.9% for the experimental model and 78–99.5% for the thermodynamic model) (Figs. 1b and c). Integrating each instantaneous floatation cumulate curve yields the $\delta^{44/40}$Ca of cumulative floatation cumulates of each run. We compare the modeled $\delta^{44/40}$Ca of cumulative floatation cumulates of each run with a simulated value from the observed highland $\delta^{44/40}$Ca range to determine whether they agree. These simulated values (10,000) are drawn from Gaussian distributions using the mean $\delta^{44/40}$Ca of highland FANs and breccias (0.763 ± 0.044‰, 2SD). Their absolute deviations from the mean (0.763‰) are recorded and randomly paired with the modeled $\delta^{44/40}$Ca values of cumulative floatation cumulates. For each modeled $\delta^{44/40}$Ca value of cumulative floatation cumulates, only when its absolute difference from the highland mean (0.763‰) is smaller than its paired absolute deviation, its associated initial LMO $\delta^{44/40}$Ca is tested as positive and saved. In contrast, the other cases are negative and dropped. Figs. 1b and c show the histograms of all valid initial LMO $\delta^{44/40}$Ca out of the 10,000 simulations, where the median approximates the mean, and the 2.5 to 97.5 percentiles give the estimated 95%

confidence intervals. The best-estimated BSM $\delta^{44/40}$Ca values are 0.879 ± 0.047‰ using the experimental deep-LMO model (*3*) and 0.916 ± 0.044‰ using the thermodynamic shallow-LMO model (*4*).

2) Temperature-dependent Mg and Ca isotopic fractionation factors

Temperature-dependent fractionation factors for Mg and Ca isotopes are defined as:

$$\alpha^{26/24}\mathrm{Mg} = ({}^{26}\mathrm{Mg}/{}^{24}\mathrm{Mg}_{\mathrm{solid}})/({}^{26}\mathrm{Mg}/{}^{24}\mathrm{Mg}_{\mathrm{melt}}) \quad \textbf{(S3)}$$

$$\alpha^{44/40}\mathrm{Ca} = ({}^{44}\mathrm{Ca}/{}^{40}\mathrm{Ca}_{\mathrm{solid}})/({}^{44}\mathrm{Ca}/{}^{40}\mathrm{Ca}_{\mathrm{melt}}) \quad \textbf{(S4)}$$

The isotopic fractionation effects [e.g., $\delta^{26/24}\mathrm{Mg} = 1000(\alpha^{26/24}\mathrm{Mg}\text{-}1)$] are thought to be proportional to the inversed square of temperature [$\alpha\text{-}1 \sim (1/T)^2$]. The $\alpha^{26/24}$Mg and $\alpha^{44/40}$Ca used in this study are given in Tables 4 and 5, both of which show great consistency between constraints from natural igneous systems (*1*, *2*, and this study) and first-principles calculations (*11–13*). In more detail, for Mg isotopic fractionation factors, we use $\delta^{26/24}\mathrm{Mg}_{\mathrm{olivine\text{-}melt}}$ and $\delta^{26/24}\mathrm{Mg}_{\mathrm{ilmenite\text{-}melt}} = 1$ according to mineral measurements and interpretations from (*1*). $\delta^{26/24}\mathrm{Mg}_{\mathrm{plagioclase\text{-}melt}}$ = 0.869‰ has been determined from the analyses of plagioclase in 76535, a troctolite sample, and the whole rock sample (*1*). A crystallization temperature of 1,229°C for plagioclase in 76535 has been recently proposed (*14*). Assuming $\delta^{26/24}\mathrm{Mg}_{\mathrm{plagioclase\text{-}melt}}$ = 0.869‰ at 1,229°C, we obtain $\delta^{26/24}\mathrm{Mg}_{\mathrm{plagioclase\text{-}melt}}$ = 1.961‰ at 1,000 K (a normalizing temperature). For other Mg-bearing minerals, including orthopyroxene, clinopyroxene, and spinel, we took the averaged $\delta^{26/24}\mathrm{Mg}_{\mathrm{mineral\text{-}olivine}}$ estimates (same as $\delta^{26/24}\mathrm{Mg}_{\mathrm{mineral\text{-}melt}}$ because $\delta^{26/24}\mathrm{Mg}_{\mathrm{olivine\text{-}melt}}$ =1) from the first-principles calculations by Schauble (*11*) and Gao et al. (*12*) (Table 4).

For Ca isotopic fractionation factors of minerals, we prefer the values obtained from data regression over first-principles calculation where they are available, such as plagioclase, clinopyroxene, pigeonite, and enstatite [Table 2 in (*2*)] (Table 5). For minerals whose fractionation factors are only estimated by first-principles calculation, such as olivine, we calculate the means of estimates from various studies (Table 5). Specifically, the clinopyroxene crystallized from the experiment by Schmidt and Kraettli (*4*) was mostly low-Ca augite ($\mathrm{Wollastonite}_{20\text{-}30}$), whose $\alpha^{44/40}$Ca estimates are not currently available. However, a general inverse relationship between Ca content and the extent of pyroxene-melt Ca isotopic fractionation has been found (*2*, *15*). Based on this presumed inverse relationship, we adopt a linear interpolation between the alpha of Diopside (1.00009, $\mathrm{Wollastonite}_{40\text{-}50}$) and pigeonite (1.00044, $\mathrm{Wollastonite}_{5\text{-}20}$) (*16*) to approximate the alpha Ca of the low-Ca augite (1.000265) used for the experimental model (Table 5). Moreover, because of the minimal mass proportions and Ca concentrations of Fe-Ti oxides (<0.2 wt.%) and quartz crystallizing from the late-stage LMO, the Ca budget and Ca isotopic fractionation effects of these minerals are neglected.

For the experimental model (*3*), the MgO and CaO contents of fractionating minerals are extracted from their experimental results for each key experiment. For the thermodynamic model (*4*), the MgO and CaO concentrations of LMO cumulate minerals are estimated based on lunar mineral data (*17*). The bulk isotope fractionation factor ($\alpha^{26/24}$Mg and $\alpha^{44/40}$Ca) can then be determined using the mineral elemental concentration and isotopic fractionations factors as follows:

$$\alpha^{26/24}Mg = \sum_i X_i C^{Mg} \alpha^{26/24}Mg_{i-melt} / \sum_i X_i C^{Mg} \quad \textbf{(S5)}$$

$$\alpha^{44/40}Ca = \sum_i X_i C^{Ca} \alpha^{44/40}Ca_{i-melt} / \sum_i X_i C^{Ca} \quad \textbf{(S6)}$$

Where X_i is the mineral mass proportion in the fractionating mineral assemblage; C^{Mg} and C^{Ca} are the MgO and CaO concentrations in the mineral.

3) Mg and Ca isotopic fractionation models with a Monte Carlo method

We forward model the $\delta^{26/24}$Mg and $\delta^{44/40}$Ca evolution of the LMO with the same isotopic fractionation model used in Section 3: Inversion for the BSM Ca-isotope composition. This fractionation model is adapted from the Rayleigh fractionation Monte Carlo method developed in Fu et al. (*2*) that tracks the uncertainty propagation associated with the initial isotopic compositions and fractionation factors.

Based on the initial elemental concentration (C^i_T) and bulk partition coefficient of individual crystallization stages (D^i) (Tables 2 and 3), the MgO and CaO elemental variations (C^i_m) during the LMO crystallization are calculated. For equilibrium crystallization:

$$\frac{C^i_m}{C^i_T} = F^{(D^i - 1)} \quad \textbf{(S7)}$$

and for fractional crystallization:

$$\frac{C^i_m}{C^i_T} = \left[F + D^i\,(1 - F)\right]^{-1} \quad \textbf{(S8)}$$

Where F is the mass fraction of the remaining melt. The results are shown in Fig. 3 for the thermodynamic and experimental models. Next, we define the equations for Rayleigh isotopic fractionation during crystallization. For equilibrium crystallization, the isotopic variation of the melt (E_m) is given by:

$$\delta^{i/j}E_m = \frac{\left[1000 + \delta^{i/j}_T\right]}{\left[f^j_m + \left(1 - f^j_m\right)\alpha^{i/j}_{s/m}\right]} - 1{,}000 \quad \textbf{(S9)}$$

and for fractional crystallization it gives:

$$\delta^{i/j}E_m = \left[1000 + \delta^{i/j}_T\right]\left[f_m^{j\,(\alpha^{i/j}_{s/m} - 1)}\right] - 1{,}000 \quad \textbf{(S10)}$$

where i is the Mg/Ca isotope mass 26 or 44; j is 24 or 40; $\delta^{i/j}_T$ is the initial isotope composition of the LMO (also BSM); $\alpha^{i/j}_{s/m}$ is the fractionation factor of i/j between minerals and melts; f^j_m is the mass fraction of the reference isotope j (^{24}Mg or ^{40}Ca) in the melt, which gives:

$$f^j_m = \frac{C^j_m F}{C^j_T} \quad \textbf{(S11)}$$

For both equilibrium and fractional crystallization, the isotopic evolution of the instantaneous cumulate (E_{cum}) follows as:

$$\delta^{i/j}E_{cum} = \delta^{i/j}E_m + 1{,}000\ln\left(\alpha_{s/m}^{i/j}\right) \quad \textbf{(S12)}$$

Here we describe the workflow of the forward isotopic modeling (results shown in Figs. 2a and d). First, to set up the initial LMO isotopic values, we drew random values (N = 10,000) from normal distributions constrained by the mean and two standard errors of BSM values. For Mg isotopes, the BSM $\delta^{26/24}$Mg of -0.291 ± 0.018‰ (*1*) was used for both the thermodynamic and experimental models. For BSM $\delta^{44/40}$Ca, 0.879 ± 0.047‰ and 0.916 ± 0.044‰, inversed from the experimental (*3*) and thermodynamic (*4*) models, were applied to these two models, respectively.

Second, we simulated the bulk Mg and Ca isotopic fractionation factors considering uncertainty. Take Mg isotope for an example:

1. We drew one random $\alpha^{26/24}$Mg for each mineral from normal distributions defined by the mean and the associated 2SE (Table 4).

2. Using the mineral mass proportions and D^{Mg} from Table 2 or 3, we quantified one set of bulk $\alpha^{26/24}$Mg values for the various crystallization stages.

3. The above steps were repeated to form 10,000 sets of bulk $\alpha^{26/24}$Mg.

These 10,000 sets of bulk $\alpha^{44/40}$Ca were randomly paired with the simulated initial $\delta^{26/24}$Mg to calculate the $\delta^{26/24}$Mg evolution of melt and cumulate using equations (S9–S12). The isotopic variation was computed with an increment method to account for the changing temperature-dependent fractionation factors. We divided the degree of crystallization (1-F) of each crystallization stage into sufficiently small increments (1,000 steps). For each increment step, the corresponding crystallization temperature (T) was calculated by the degree of crystallization using the equation in Fig. 2, which was then used to obtain the bulk isotopic fractionation factors at T [e.g., ($\alpha^{26/24}$Mg$_{(T)}$-1) = ($\alpha^{26/24}$Mg-1)/(T/1,000)^2]. $\delta^{26/24}Mg_{melt}$ after each increment in 1-F was calculated using equation (S8) or (S9), which then became $\delta_T^{26/24}Mg$ of the next step. The incremental calculation stopped at the end of LMO crystallization. Repeating the calculations for all paired initial $\delta^{26/24}$Mg and bulk $\alpha^{26/24}$Mg, we obtained 10,000 modeled $\delta^{26/24}Mg_{melt}$ curves as a function of degree of LMO crystallization (Figs. 2a and d). The mean $\delta^{26/24}Mg_{melt}$ curve was obtained by averaging all modeled $\delta^{26/24}Ca_{melt}$ values at each incremental step. The 95% confidence intervals at each step were estimated to be the 2.5 to 97.5 percentiles of the modeled values. $\delta^{26/24}Mg_{cum}$ was calculated from $\delta^{26/24}Mg_{melt}$ using equation (S12).

The calculation method described above was similarly applied to modeling $\delta^{44/40}$Ca with both experimental (Fig. 2a) and thermodynamic (Fig. 2d) LMO crystallization models.

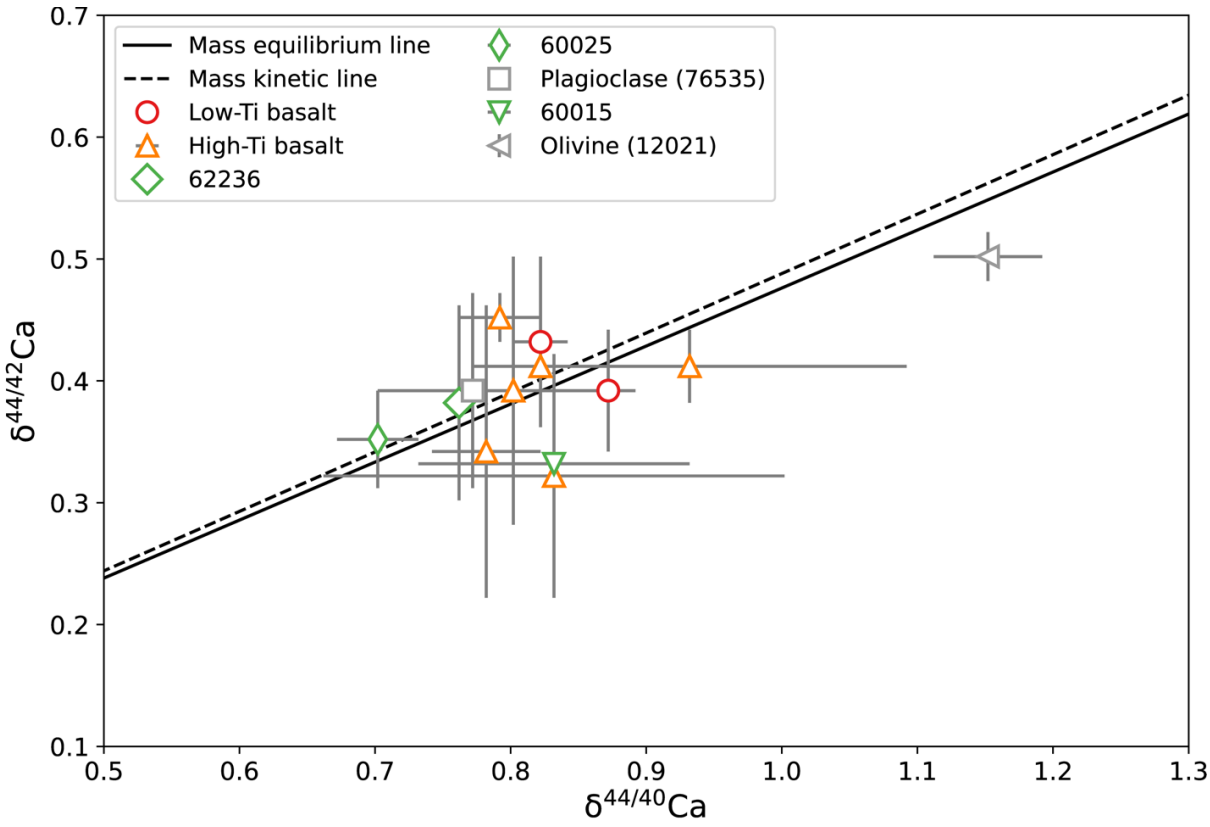

185

186 **Fig. 1. $\delta^{44/42}$Ca vs. $\delta^{44/40}$Ca (relative to SRM915a) of analyzed lunar rocks and minerals.** The
187 mass-dependent equilibrium line is defined by a slope of 2.0995^{-1}, while the kinetic line has a slope
188 of 2.0483^{-1} (*18*).

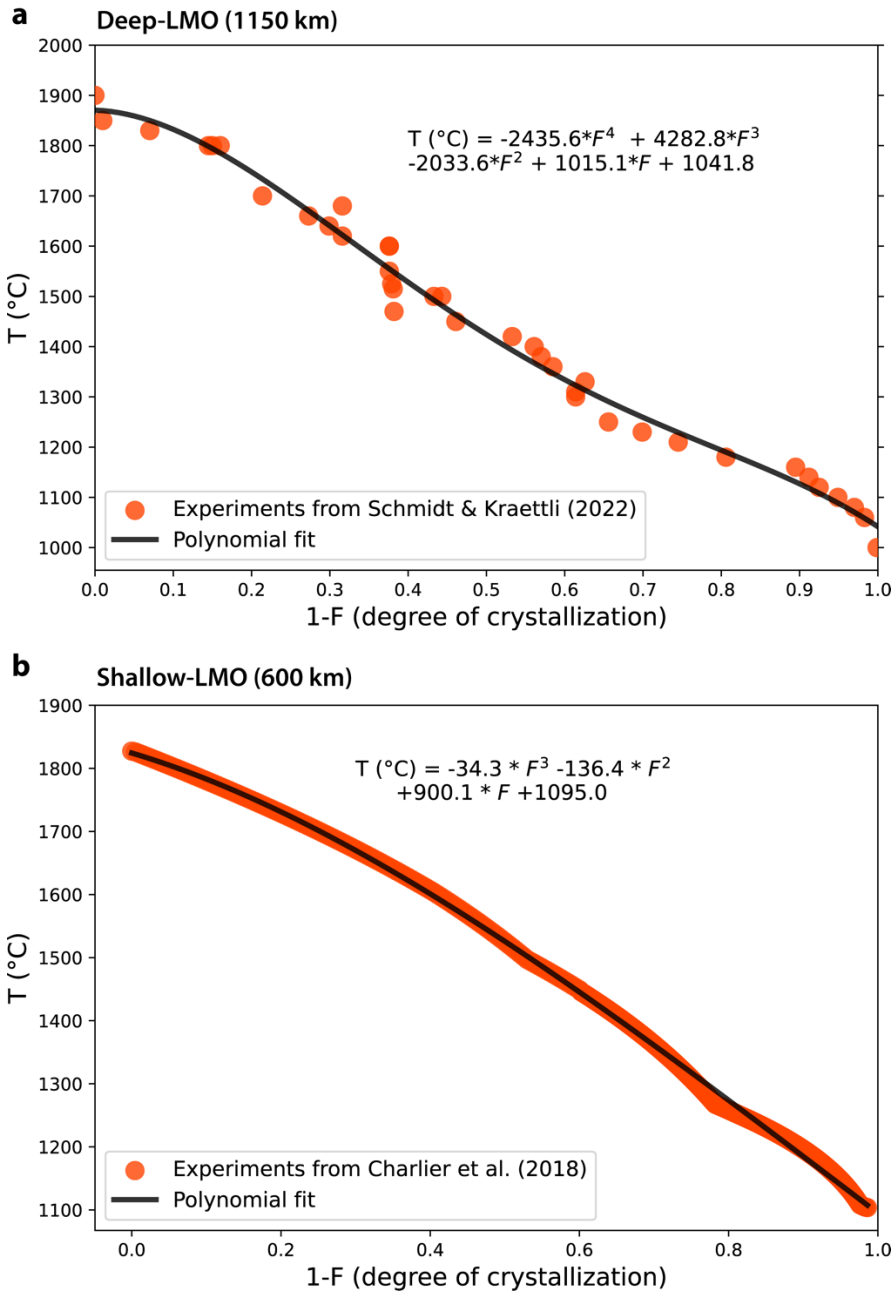

Fig. 2. LMO crystallization temperature as a function of degree of crystallization for deep (*3*) and shallow (*7*) conditions. The polynomial fit is expressed at the top of each diagram (equation S1 and S2).

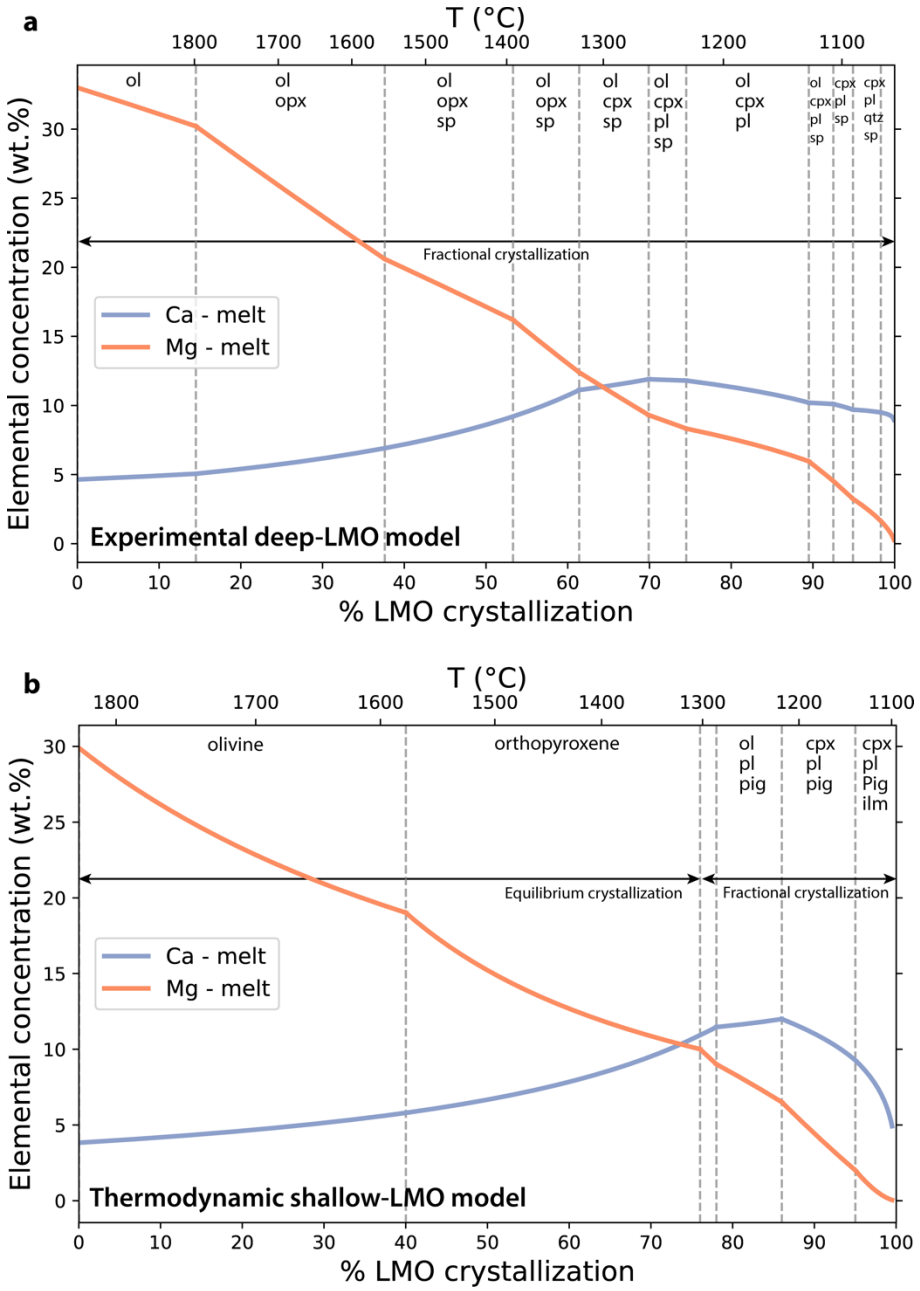

Fig. 3. Ca and Mg variations throughout the LMO crystallization. (**a**) Elemental variations analyzed by the experiments assuming solely fractional crystallization for a deep LMO (*3*). (**b**) Elemental variations calculated by the thermodynamic shallow-LMO model considering the first 76% solidification as equilibrium crystallization and the rest as fractional crystallization (*4*). The mineral abbreviations on top of the diagram signify the fractionating phases of each crystallization stage: ol—olivine; opx—orthopyroxene; pig—pigeonite; cpx—clinopyroxene; pl—plagioclase; ilm—ilmenite; sp—spinel; qtz—quartz.

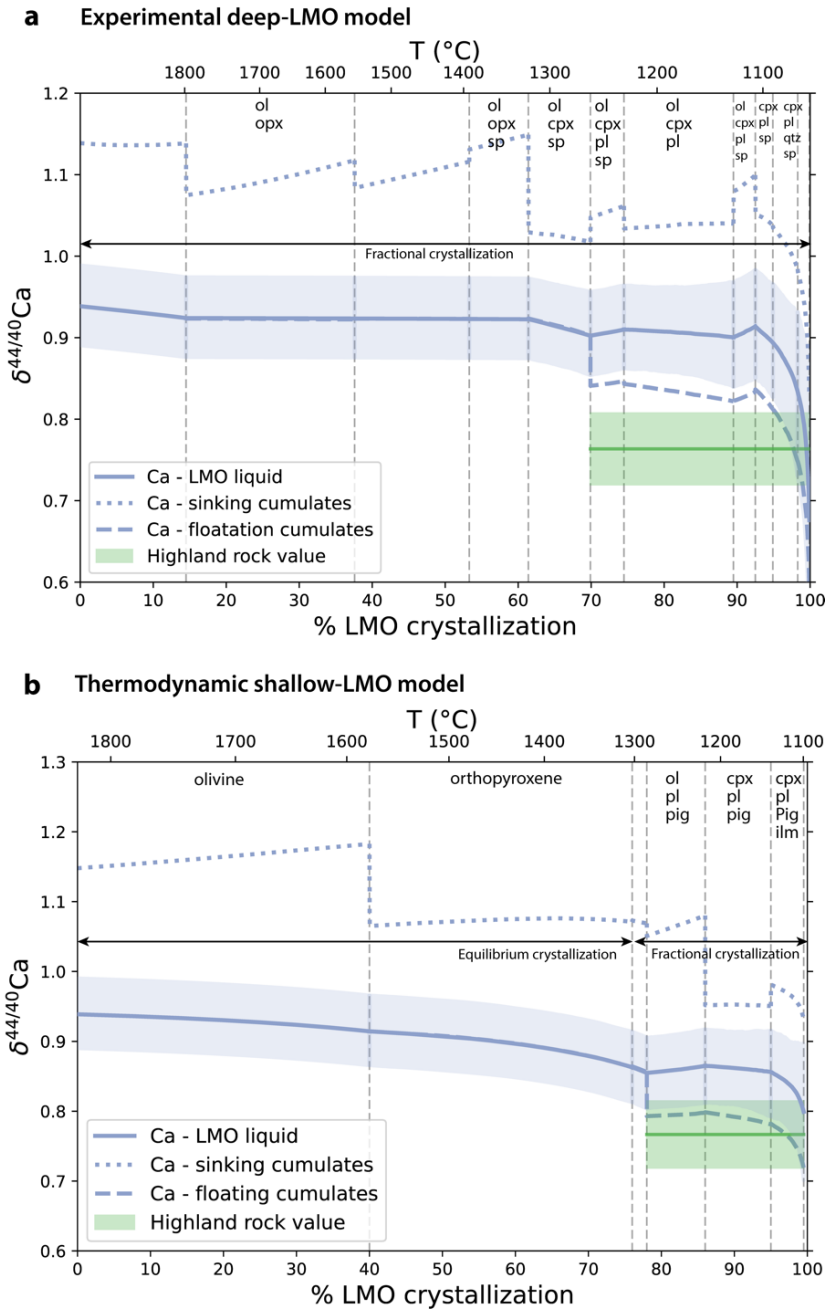

Fig. 4. $\delta^{44/40}$Ca evolution of the LMO assuming an initial BSM $\delta^{44/40}$Ca identical to the BSE (0.94 ± 0.05‰) (*9*). (**a**) $\delta^{44/40}$Ca evolution calculated with the experimental model (*4*). (**b**) $\delta^{44/40}$Ca evolution calculated with the thermodynamic model (*3*). The blue curves show the mean evolution paths (melt, sinking, and floatation cumulates). The color field surrounding the melt curve represents the 95% confidence intervals determined by the Monte Carlo approach, considering uncertainties in the initial isotopic composition and mineral fractionation factors. The fractionating mineral abbreviations are the same as in Fig. 3.

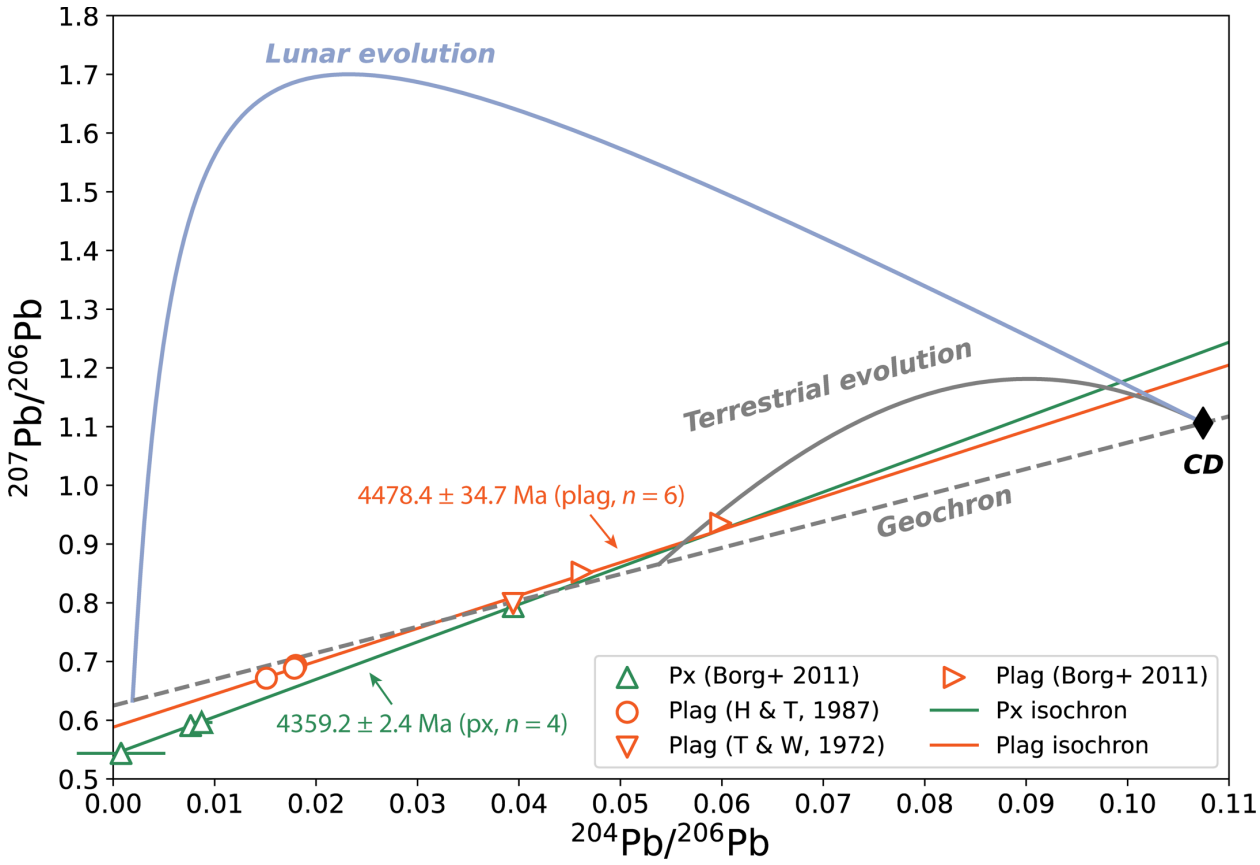

213

214 **Fig. 5. $^{207}Pb/^{206}Pb$–$^{204}Pb/^{206}Pb$ isochron for plagioclase and pyroxene of 60025.** Pb data are
215 from (*19–21*). The isochron for plagioclase is calculated using IsoplotR (*22*). The isochron for
216 pyroxene is from (*20*). *CD* denotes the solar-system initial Pb composition represented by Canyon
217 Diablo troctolite (*23*).The Pb-Pb evolution curves are calculated assuming μ-value ($^{238}U/^{204}Pb$) =
218 9 for the Earth and μ = 500 for the Moon (*24*). For the figure legend: H & T, 1987—ref. (*19*);
219 Borg+ 2011—ref. (*20*); T & W, 1972—ref. (*21*); Px—pyroxene; Plag—plagioclase.

220

Table 1
Ca isotope compositions of analyzed lunar rocks and minerals.

Sample	$\delta^{44/40}$Ca measured		$\delta^{44/42}$Ca measured		$\delta^{44/40}$Ca calculated by $\delta^{44/42}$Ca[(b)]		Weighted mean $\delta^{44/40}$Ca[(c)]	
	$\delta^{44/40}$Ca	± 2SE[(a)]	$\delta^{44/42}$Ca	± 2SE	$\delta^{44/40}$Ca	± 2SE	$\delta^{44/40}$Ca	± 2SE
Lunar rocks								
Low-Ti basalt								
12002, 122 (olivine basalt)	0.822	0.020	0.432	0.070	0.885	0.143	0.823	0.020
15555, 19	0.872	0.020	0.392	0.050	0.803	0.102	0.869	0.020
High-Ti basalt								
10017, 282 (ilmenite basalt)	0.782	0.040	0.342	0.120	0.701	0.246	0.780	0.039
70035, 200 (ilmenite basalt)	0.832	0.050	0.322	0.100	0.660	0.205	0.822	0.049
71569, 69 (ilmenite basalt)	0.822	0.010	0.412	0.040	0.844	0.082	0.822	0.010
10044, 652 (ilmenite basalt)	0.802	0.050	0.392	0.110	0.803	0.225	0.802	0.049
74275, 344 (ilmenite basalt)	0.932	0.160	0.412	0.030	0.844	0.061	0.855	0.057
70215	0.792	0.030	0.452	0.020	0.926	0.041	0.839	0.024
Highland rock								
60025, 901 (ferroan anorthosite)	0.702	0.030	0.352	0.040	0.721	0.082	0.704	0.028
62236, 64 (ferroan anorthosite)	0.762	0.010	0.382	0.080	0.782	0.164	0.762	0.010
60015, 761 (cataclastic anorthosite)	0.832	0.100	0.332	0.070	0.680	0.143	0.782	0.082
Lunar minerals								
Olivine (low-Ti basalt 12021)	1.152	0.040	0.502	0.020	1.028	0.041	1.092	0.029
Plagioclase (troctolite 76535)	0.772	0.070	0.392	0.080	0.803	0.164	0.777	0.064

Notes:

[(a)]2SE: two standard errors.

[(b)]assuming a mass-dependent fractionation relationship, $\delta^{44/40}Ca \approx 2.0483 * \delta^{44/42}Ca$ (*18*).

[(c)]weighted mean of the measured $\delta^{44/40}$Ca and calculated $\delta^{44/40}$Ca (by $\delta^{44/42}$Ca); the weight of each is given by $2SE^{-2}$.

221

Table 2

Parameters for the LMO isotopic fractionation model [thermodynamic shallow-LMO model by Snyder et al. (4)].

Isotope	Crystallization Stage	BSM elemental concentration (wt.%)	BSM isotopic composition	BSM 2SE	Crystallization	Degree of LMO crystallization	Fractionating mineral	Bulk *D*-value	Bulk α [(a)]	α of sinking cumulates [(b)]	α of flotation cumulates [(c)]	2SE of bulk α [(d)]
$\delta^{26/24}$Mg		29.9	-0.291	0.018								
	1				Equlibrium	0–40%	olivine	2.43	1	1	-	0
	2				Equlibrium	0–76%	orthopyroxene	2.50	1.000113	1.000113	-	0
	3				Equlibrium	76–78%	orthopyroxene	2.20	1.000113	1.000113	-	0
	4				Fractional	78–86%	25% olivine + 53% plagioclase +22% pigeonite	1.72	1.000079	1.000052	1.001961	2.03E-06
	5				Fractional	86–95%	38% clinopyroxene + 36% plagioclase +26% pigeonite	2.14	1.000158	1.000138	1.001961	1.68E-06
	6				Fractional	95–99.5%	34% pigeonite + 31% plagioclase +24% plagioclase + 11% ilmenite	2.60	1.000154	1.000137	1.001961	1.46E-06
$\delta^{44/40}$Ca		3.83	0.916	0.044								
	1				Equlibrium	0–40%	olivine	0.15	1.000920	1.000920	-	0
	2				Equlibrium	0–76%	orthopyroxene	0.22	1.000520	1.000520	-	1.000E-04
	3				Equlibrium	76–78%	orthopyroxene	0.45	1.000520	1.000520	-	1.000E-04
	4				Fractional	78–86%	25% olivine + 53% plagioclase +22% pigeonite	0.90	0.999939	1.000476	0.999850	7.074E-05
	5				Fractional	86–95%	38% clinopyroxene + 36% plagioclase +26% pigeonite	1.25	1.000014	1.000190	0.999850	5.115E-05
	6				Fractional	95–99.5%	34% pigeonite + 31% plagioclase +24% plagioclase + 11% ilmenite	1.28	1.000038	1.000247	0.999850	5.359E-05

Notes:

[(a)] Bulk α is caluclated by the mineral isotopic fractionation factors (Table 4 and 5) and elemental concentration (Table 6) using equation (S5 and S6).

[(b)] α of sinking cumulates is the bulk average of heavy minerals including olivine, pyroxene, and Fe-Ti oxide.

[(c)] α of floatation cumulates denotes plagioclase.

[(d)] The two standard errors (2SE) of the bulk α is calculated using standard error propagation.

Table 3

Parameters for the LMO isotopic fractionation model [experimental deep-LMO model by Schmidt and Kraettli (3)].

Isotope	Crystallization Stage	BSM elemental concentration (wt.%)	BSM isotopic composition	BSM 2SE	Crystallization	Degree of LMO crystallization	Fractionating mineral	Bulk *D*-value	Bulk α [(a)]	α of sinking cumulates [(b)]	α of flotation cumulates [(c)]	2SE of bulk α [(d)]
$\delta^{26/24}$Mg		33	-0.291	0.018								
	1				Fractional	0–14.5%	100% olivine	1.57	1	1	-	0
	2				Fractional	14.5–37.6%	73% olivine + 27% orthopyroxene	2.22	1.000021	1.000021	-	0
	3				Fractional	37.6–53.3%	12% olivine + 82% orthopyroxene + 6% spinel	1.83	1.000122	1.000122	-	0
	4				Fractional	53.3–61.4%	48% olivine + 52% orthopyroxene + 1% spinel	2.41	1.000048	1.000048	-	0
	5				Fractional	61.4–69.9%	26% olivine + 65% clinopyroxene + 9% spinel	2.15	1.000124	1.000124	-	0
	6				Fractional	69.9–74.5%	34% olivine + 7% clinopyroxene + 59% plagioclase + 1% spinel	1.67	1.000044	1.000025	1.001961	1.42E-06
	7				Fractional	74.5–89.5%	15% olivine + 35% clinopyroxene + 50% plagioclase	1.38	1.000102	1.000076	1.001961	2.02E-06
	8				Fractional	89.5–92.5%	35% olivine + 9% clinopyroxene + 53% plagioclase + 4% spinel	1.82	1.000049	1.000028	1.001961	1.61E-06
	9				Fractional	92.5–94.9%	53% clinopyroxene + 31% plagioclase + 16% spinel	1.87	1.000189	1.000178	1.001961	8.97E-07
	10				Fractional	94.9–98.3%	44% clinopyroxene + 28% plagioclase + 21% spinel + 6% quartz	1.62	1.000198	1.000181	1.001961	1.40E-06
	11				Fractional	98.3–99.9%	44% clinopyroxene + 28% plagioclase + 21% spinel + 6% quartz	1.62	1.000198	1.000181	1.001961	1.40E-06
$\delta^{44/40}$Ca		4.64	0.879	0.047								
	1				Fractional	0–14.5%	100% olivine	0.45	1.000920	1.000920	-	0
	2				Fractional	14.5–37.6%	73% olivine + 27% orthopyroxene	0.01	1.000649	1.000649	-	6.772E-05
	3				Fractional	37.6–53.3%	12% olivine + 82% orthopyroxene + 6% spinel	0.01	1.000529	1.000529	-	9.775E-05
	4				Fractional	53.3–61.4%	48% olivine + 52% orthopyroxene + 1% spinel	0.01	1.000574	1.000574	-	8.639E-05
	5				Fractional	61.4–69.9%	26% olivine + 65% clinopyroxene + 9% spinel	0.726	1.000271	1.000271	-	1.734E-04
	6				Fractional	69.9–74.5%	34% olivine + 7% clinopyroxene + 59% plagioclase + 1% spinel	1.05	0.999898	1.000341	0.999850	7.376E-05
	7				Fractional	74.5–89.5%	15% olivine + 35% clinopyroxene + 50% plagioclase	1.164	1.000020	1.000274	0.999850	8.426E-05
	8				Fractional	89.5–92.5%	35% olivine + 9% clinopyroxene + 53% plagioclase + 4% spinel	1.029	0.999926	1.000355	0.999850	7.166E-05
	9				Fractional	92.5–94.9%	53% clinopyroxene + 31% plagioclase + 16% spinel	1.105	1.000084	1.000265	0.999850	1.046E-04
	10				Fractional	94.9–98.3%	44% clinopyroxene + 28% plagioclase + 21% spinel + 6% quartz	1.02	1.000096	1.000265	0.999850	1.089E-04
	11				Fractional	98.3–99.9%	44% clinopyroxene + 28% plagioclase + 21% spinel + 6% quartz	1.02	1.000096	1.000265	0.999850	1.089E-04

Notes:

[(a)] Bulk α is caluclated by the mineral isotopic fractionation factors (Table 4 and 5) and elemental concentration (Table 6) using equation (S5 and S6).

[(b)] α of sinking cumulates is the bulk average of heavy minerals including olivine, pyroxene, and Fe-Ti oxide.

[(c)] α of floatation cumulates denotes plagioclase.

[(d)] The two standard errors (2SE) of the bulk α is calculated using standard error propagation.

223

Table 4

Mineral-melt isotopic fractionation factor for $^{26}Mg/^{24}Mg$.

Mineral	$\alpha^{26/24}Mg$	$\delta^{26/24}Mg$	2SE ($\delta^{26/24}Mg$)	Reference	Notes
Olivine	1	0.000	-	(*1*)	
Orthopyroxene	1.000113	0.113	-	(*11*, *12*)	Averaged value from both studies
Pigeonite	1.000138	0.138	-	(*11*, *12*)	Assuming that the pigeonite fractionation factor is similar to that of clinopyroxene
Clinopyroxene	1.000138	0.138	-	(*11*, *12*)	Averaged value from both studies
Plagioclase[(a)]	1.001961	1.961	0.150	(*1*)	Converted to 1,000 K assuming a $\delta^{26/24}Mg_{plagioclase\text{-}melt}$ = 0.869‰ at 1,229°C (*14*)
Ilmenite	1	0.000	-	(*1*)	
Spinel	1.000956	0.956	-	(*11*, *12*)	Averaged value from both studies

Notes:

All $\alpha^{26/24}Mg$ and $\delta^{26/24}Mg$ presneted in the table are for 1,000 K.

[(a)]The $\delta^{26/24}Mg$ 2SE for plagioclase is quantified by the propagated error of the diffrence between the measured plagioclase separate and whole-rock 76535 considering their analytical uncertainties.

224

Table 5

Mineral-melt isotopic fractionation factor for $^{44}Ca/^{40}Ca$.

Mineral	$\alpha^{44/40}Ca$	$\delta^{44/40}Ca$	2SE ($\delta^{44/40}Ca$)	Reference	Notes
Olivine	1.000920	0.920	-	(*13* , *25*)	Averaged value from both studies
Orthopyroxene	1.000520	0.520	0.1	(*16*)	
Pigeonite	1.000440	0.440	0.13	(*16*)	
Clinopyroxene	1.000090	0.090	0.07	(*16*)	
Clinopyroxene (low-Ca augite)	1.000265	0.265	0.175[(a)]	(*16*)	Interpolated value from clinopyroxene and pigeonite
Plagioclase	0.999850	-0.150	0.08	(*16*)	

Notes :

All $\alpha^{44/40}Ca$ and $\delta^{44/40}Ca$ presneted in the table are for 1,000 K.

225 [(a)]The $\delta^{44/40}Ca$ 2SE for low-Ca augite is assuming the mean $\delta^{44/40}Ca = 0.265$ and a 95% confidence interval between $\delta^{44/40}Ca = 0.09$ (diopside) and $\delta^{44/40}Ca = 0.44$ (pigeonite).

Table 6

Estimated elemental concentration of fractionating minerals [for Snyder et al. (*4*) model].

Mineral	MgO (wt.%)	CaO (wt.%)
Olivine	49	0.5
Pigeonite	32	7
Clinopyroxene	20	12
Plagioclase	0.5	19
Ilmenite	1	0.2

Notes:

226 Estimates are based on lunar mineral compositions from Papike et al. (*17*).

Table 7
Geochronologic constraints for the short-lived LMO model.

Description	Age (Ma)	Uncertainty (Ma)	% of LMO crystallization	Uncertainty (%)	Age reference
Hf-W isotopic modeling	4537	-	0	-	Yu and Jacobsen (*26*)
$^{182}W/^{184}W$ isotope data (the silicate Moon)	4517	10	0	-	Thiemens et al. (27)
$^{182}W/^{184}W$ isotope data (lunar metal)	4517	+10/-90	0	-	Touboul et al. (*28*); Nemchin et al. (*34*)
Hf model age of zircon	4510	10	0	-	Barboni et al. (*29*)
60025 (anorthosite)	4510	10	99[(b)]	1	Hanan and Tilton (*19*)
72415 (lunar dunite)	4527[(a)]	92	40[(b)]	40	Papanastassiou and Wasserburg (*30*)
Formation of KREEP source (old estimate)	4456	65	94	1	Borg et al. (*20*)

Notes:
[(a)]The mean age of the sample is re-calculated from the original data using the new ^{87}Rb-^{87}Sr decay constant [1.397 x 10^{-11} yr^{-1}, Rotenberg et al. (*31*)].
[(b)]The constraint on the % of LMO crystallization is from this study.

227

Table 8

Geochronologic constraints for the Long-lived LMO Model.

Description	Age (Ma)	Uncertainty (Ma)	% of LMO crystallization	Uncertainty (%)	Age reference
Hf-W isotopic modeling	4537	-	0	-	Yu and Jacobsen (*26*)
$^{182}W/^{184}W$ isotope data (the silicate Moon)	4517	10	0	-	Thiemens et al. (27)
$^{182}W/^{184}W$ isotope data	4517	+10/-90	0	-	Touboul et al. (*28*); Nemchin et al. (*34*)
Hf model age of zircon	4510	10	0	-	Barboni et al. (*29*)
60025 (anorthosite)	4383	17	99[(b)]	1	Borg. et al. (*32*)
72415 (lunar dunite)	4527[(a)]	92	40[(b)]	40	Papanastassiou and Wasserburg (*30*)
Average FANs age	4456	40	89[(c)]	11	Norman et al. (*33*)
U-Pb lunar zircon age	4417	6	94	1	Nemchin et al. (*34*)
Formation of KREEP source (old estimate)	4456	65	94	1	Borg et al. (*20*)
Formation of KREEP source (young estimate)	4368	29	94	1	Gaffney and Borg (*35*)

Notes:

[(a)]The mean age of the sample is re-calculated from the original data using the new ^{87}Rb-^{87}Sr decay constant [1.397 x 10^{-11} yr^{-1}, Rotenberg et al. (*31*)].

[(b)]The constraint on the % of LMO crystallization is from this study.

[(c)]The constraint on the % of LMO crystallization is based on Snyder et al. (*4*), which resolved the lunar anorthosite formation between 78% and 100% LMO solidification.

228

Supplementary References

1. F. Sedaghatpour, S. B. Jacobsen, Magnesium stable isotopes support the lunar magma ocean cumulate remelting model for mare basalts. *Proc. Natl. Acad. Sci.* **116**, 73–78 (2019).
2. H. Fu, S. B. Jacobsen, B. T. Larsen, Z. Eriksen, Ca-isotopes as a robust tracer of magmatic differentiation. *Earth and Planetary Science Letters*. **594**, 117743 (2022).
3. M. W. Schmidt, G. Kraettli, Experimental Crystallization of the Lunar Magma Ocean, Initial Selenotherm and Density Stratification, and Implications for Crust Formation, Overturn and the Bulk Silicate Moon Composition. *J. Geophys. Res.: Planets **127***, (2022).
4. G. A. Snyder, A. Taylor, C. R. Neal, A chemical model for generating the sources of mare basalts : Combined equilibrium and fractional crystallization of the lunar magmasphere. *Geochim. Cosmochim. Acta* **56**, 3809–3823 (1992).
5. S. R. Taylor, Planetary science: A lunar perspective. *Lunar and Planetary Institute* (1982).
6. Y. Lin, E. J. Tronche, E. S. Steenstra, W. van Westrenen, Evidence for an early wet Moon from experimental crystallization of the lunar magma ocean. *Nat. Geosci.* **10**, 14–18 (2017).
7. B. Charlier, T. L. Grove, O. Namur, F. Holtz, Crystallization of the lunar magma ocean and the primordial mantle-crust differentiation of the Moon. *Geochim. Cosmochim. Acta* **234**, 50–69 (2018).
8. J. F. Rapp, D. S. Draper, Fractional crystallization of the lunar magma ocean: Updating the dominant paradigm. *Meteoritics & Planetary Sciences **53***, 1432–1455 (2018).
9. J.-T. Kang, D. A. Ionov, F. Liu, C.-L. Zhang, A. V. Golovin, L.-P. Qin, Z.-F. Zhang, F. Huang, Calcium isotopic fractionation in mantle peridotites by melt- ing and metasomatism and Ca isotope composition of the Bulk Silicate Earth. *Earth Planet. Sci. Lett.* **474**, 128–137. (2017).
10. K. Wang, S. B. Jacobsen, F. Sedaghatpour, H. Chen, R. L. Korotev, The earliest lunar magma ocean differentiation recorded in Fe isotopes. *Earth Planet Sci. Lett.* **430**, 202–208 (2015).
11. E. A. Schauble, First-principles estimates of equilibrium magnesium isotope fractionation in silicate, oxide, carbonate and hexaaquamagnesium(2+) crystals. *Geochimica et Cosmochimica Acta **75***, 844–869 (2011).
12. C. Gao, X. Cao, Q. Liu, Y. Yang, S. Zhang, Y. He, M. Tang, Y. Liu, Theoretical calculation of equilibrium Mg isotope fractionations between minerals and aqueous solutions. *Chemical Geology **488***, 62–75 (2018).
13. M. A. Antonelli, M. Schiller, E. A. Schauble, T. Mittal, D. J. DePaolo, T. Chacko, E. S. Grew, B. Tripoli, Kinetic and equilibrium Ca isotope effects in high-T rocks and minerals. *Earth Planet. Sci. Lett.* **517**, 71–82 (2019).
14. W. S. Nelson, J. E. Hammer, T. Shea, E. Hellebrand, T. G. Jeffrey, Chemical heterogeneities reveal early rapid cooling of Apollo Troctolite 76535. *Nat. Commun. **12**, 7054* (2021).
15. M. A. Antonelli, J. I. Simon, Calcium isotopes in high-temperature terrestrial processes. *Chem. Geol.* **548**, 119–651 (2020).
16. H. Zhang, Y. Wang, Y. He, F.-Z. Teng, S. B. Jacobsen, R. T. Helz, B. D. Marsh, S. Huang, No measurable calcium isotopic fractionation during crystallization of Kilauea Iki Lava Lake. *Geochem. Geophys. Geosyst.* **19**, 3128–3131 (2018).
17. Papike J., Taylor L., Simon S. Lunar Sourcebook, A User's Guide to Moon. *Cambridge: Cambridge Univ. Press* **121** (1991).

18. E. D. Young, A. Galy, H. Nagahara, Kinetic and equilibrium mass-dependent isotope fractionation laws in nature and their geochemical and cosmochemical significance. *Geochim. Cosmochim. Acta* **66**, 1095–1104 (2002).
19. B. B. Hanan, G. R. Tilton, 60025: relict of primitive lunar crust? *Earth Planet Sci. Lett.* ***84***, 15–21 (1987).
20. L. E. Borg, J. N. Connelly, M. Boyet, R.W. Carlson, Chronological evidence that the Moon is either young or did not have a global magma ocean. *Nature* ***477***, 70–72 (2011).
21. F. Tera, G. J. Wasserburg, U-Th-Pb systematics in lunar highland samples from the Luna 20 and Apollo 16 missions. *Earth Planet Sci. Lett.,* **17**, 36-51 (1972).
22. P. Vermeesch, IsoplotR: A free and open toolbox for geochronology. *Geosci. Front.* **9**, 1479–1493 (2018).
23. M. Tatsumoto, R. J. Knight, C. J. Allègre, Time Differences in the Formation of Meteorites as Determined from the Ratio of Lead-207 to Lead-206. *Science* **180**, 1279–1283 (1973).
24. Connelly, J.N., Nemchin, A., Merle, R.E., Snape, J.F., Whitehouse, M.J., & Bizzarro, M. (2022). Calibrating volatile loss from the Moon using the U-Pb system. *Geochim. Cosmochim. Acta* **324**, 1–16 (2022).
25. F. Huang, C. Zhou, W. Wang, J. Kang, Z. Wu, First-principles calculations of equilibrium Ca isotope fractionation: Implications for oldhamite formation and evolution of lunar magma ocean. *Earth Planet. Sci. Lett.* **510**, 153–160 (2019).
26. G. Yu, S. B. Jacobsen, Fast accretion of the Earth with a late Moon-forming giant impact. *Proc. Natl. Acad. Sci.* ***108***, 17604–17609 (2011).
27. M. M. Thiemens, P. Sprung, R. O. Fonseca, F. P. Leitzke, C. Münker, Early Moon formation inferred from hafnium–tungsten systematics. *Nat. Geosci.* **12**, 696–700 (2019).
28. M. Touboul, T. Kleine, B. Bourdon, H. Palme, R. Wieler, Late formation and prolonged differentiation of the Moon inferred from W isotopes in lunar metals. *Nature* ***450***, 1206–1209 (2007).
29. M. Barboni, P. Boehnke, B. Keller, I. E. Kohl, B. Schoene, E. D. Young, K. D. McKeegan, Early formation of the Moon 4.51 billion years ago. *Sci. Adv.* ***3***, 1602365 (2017).
30. D. A. Papanastassiou, G. J. Wasserburg, Rb-Sr study of a lunar dunite and evidence for early lunar differentiates. *Proc. 6th Lunar Sci. Conf.* 1467–1489 (1975).
31. Rotenberg, E., Davis, D.W., Amelin, Y., Ghosh, S., & Bergquist, B.A. (2012). Determination of the decay-constant of ^{87}Rb by laboratory accumulation of ^{87}Sr. *Geochimica et Cosmochimica Acta* ***85***, 41–57.
32. L. E. Borg, J. N. Connelly, W. S. Cassata, A. M. Gaffney, M. Bizzarro, Chronologic implications for slow cooling of troctolite 76535 and temporal relationships between the Mg-suite and the ferroan anorthosite suite. *Geochimica et Cosmochimica Acta* ***201***, 377–391 (2017).
33. M. D. Norman, L. E. Borg, L. E. Nyquist, D. D. Bogard, Chronology, geochem- istry, and petrology of a ferroan noritic anorthosite clast from Descartes brec- cia 67215: clues to the age, origin, structure, and impact history of the lunar crust. *Meteorit. Planet. Sci.* **38**, 645–661 (2003).
34. A. A. Nemchin, N. E. Timms, R. T. Pidgeon, T. Geisler, S. M. Reddy, C. Meyer, Timing of crystallization of the lunar magma ocean constrained by the oldest zircon. *Nat. Geosci.* ***2***, 133–136 (2009).
35. A. M. Gaffney, L. E. Borg, A young solidification age for the lunar magma ocean. *Geochim. Cosmochim. Acta* ***140***, 227–240 (2014).